chemical interaction; coincubation with rAIM followed by removal of rAIM via column purification did not alter their ability to induce 3T3-L1 cell differentiation (Figure S7).

Consistent with these morphologic results, cells cultured in the presence of rAIM or C75 showed a marked decrease in mRNA levels of C/EBPα and PPARγ (γ1 and γ2), the master regulator genes for adipogenesis (Rosen et al., 1999; Wu et al., 1999a; Farmer, 2006), as well as of downstream genes characteristic of functional adipocytes, such as CD36 and GLUT4, compared to cells differentiated in the absence of rAIM or C75 (Figure 7C). Altogether, these results indicate that AIM affected adipocytes by inhibiting FAS activity.

Inhibition of FAS Did Not Activate cAMP-Dependent Lipolysis

During periods of energy deprivation, adipocytes undergo lipolysis via stimulation of a G protein-coupled receptor/cyclic AMP (cAMP)-dependent signaling cascade, followed by phosphorylation of protein kinase A (PKA), which activates hormone-sensitive lipase (HSL). At the same time, the level of adipose triglyceride lipase (ATGL) mRNA also increases (Wu et al., 1999b; He et al., 2003; Holm, 2003; Finn and Dice, 2006; Zechner et al., 2005; Duncan et al., 2007; Lafontan, 2008). Interestingly, however, despite the lipolytic consequences, treatment of 3T3-L1 adipocytes with rAIM or C75 did not upregulate the phosphorylation of PKA (Figure S8A). In addition, the levels of ATGL and HSL mRNA did not increase in response to AIM (Figure S8B). Thus, unlike in a starved situation, inhibition of FAS does not stimulate cAMP/PKA-dependent lipolysis. Note that the level of phosphorylation of 5'-AMP-activated kinase (AMPK), another element downstream of cAMP signaling whose activation inhibits HSL activity, was also not increased by AIM or C75 (Figure S8C).

DISCUSSION

A Role of AIM in Adipocytes

Our present results provide several findings regarding the influence of AIM on adipocytes. First, AIM is endocytosed into adipocytes via CD36. Second, incorporated AIM binds to cytosolic FAS protein at various regions responsible for elongation of fatty acids, release of synthesized palmitate, and stabilization of FAS

dimerization. This results in a decrease in FAS enzymatic activity. Third, the decrease in FAS activity induced by AIM results in a decrease in lipid droplet storage within adipocytes. Finally, the size of adipocytes in visceral fat tissue is increased in $AIM^{-/-}$ mice compared to $AIM^{+/+}$ mice. The physiologic consequence of the lipolytic response induced by AIM remains to be investigated. It is possible that AIM resists augmentation of adipose tissue mass, leading to decreased progression of obesity. Indeed, the increase in weight of visceral fat in mice fed with a HFD was accelerated in $AIM^{-/-}$ mice compared to $AIM^{+/+}$ mice (Figure 5B), and it was suppressed by the systemic administration of rAIM (Figure 5C). Importantly, this antiadiposity function of AIM appears to be exerted specifically via its effect on adipocytes, because both $AIM^{-/-}$ and $AIM^{+/+}$ mice showed comparable metabolic rates (Figure S5). Additional discussion related to this issue appears in the Supplemental Information online.

Direct Function of AIM in the Absence of Signaling

Interestingly, exogenous AIM secreted by macrophages is incorporated into adipocytes and directly functions intracellularly. Such a direct manner of function in the absence of signaling is unusual in a secreted molecule. However, examples in which cytosolic delivery of exogenous proteins mediates biological effects have recently been accumulating. Fibroblast growth factor (FGF)-1 and -2 (Olsnes et al., 2003; Wesche et al., 2006) as well as epidermal growth factor (EGF) (Lin et al., 2001) are transported to the cytosol after internalization via specific receptors, where they trigger cellular events. In addition, many plant and bacterial toxins, such as ricin and Shiga toxin, are also endocytosed by eukaryotic cells in a receptor-dependent manner and are translocated into the cytosol to target-specific intracellular proteins (Sandvig and van Deurs, 2000, 2005). It is also known that in dendritic cells, some exogenous antigens can access the cytosol via similar machineries for intracellular transport and are presented by major histocompatibility complex (MHC) class I (Ackerman et al., 2005; Giodini and Cresswell, 2008). Yet it remains unclear how AIM is translocated from endosomal compartments to the cytosol. Interestingly, incorporated AIM colocalized with early endosomes but not with late or recycling endosomes (Figure 3B). This observation implicates the presence of a specific mechanism to transport AIM from endosomes

---

Figure 3. AIM Is Endocytosed via CD36

(A) Differentiated 3T3-L1 adipocytes (ins/DEX/IBMX stimulation +) or undifferentiated 3T3-L1 preadipocytes without maturation stimulation (ins/DEX/IBMX stimulation −) were incubated with rAIM (5 μg/ml) for 3 hr and stained for AIM (red), PPARγ2 (green), and DAPI (blue). Top panels, AIM + DAPI; middle panels, AIM + PPARγ2; bottom panels, AIM + PPARγ2 + DAPI (merged), overlaid with phase-contrast images. In the bottom panels, cells showing strong PPARγ2 positivity contained many lipid droplets. Yellow arrows, mature 3T3-L1 adipocytes showing strong staining for PPARγ2; blue arrows, cells showing faint staining for PPARγ2; white arrows, cells showing undetectable staining for PPARγ2. Right lane (pre): undifferentiated 3T3-L1 preadipocytes without stimulation. The percentage of cells showing AIM incorporation was calculated for 100 cells of each type (graph under photomicrographs; rAIM incorporation). Results were obtained from three independent experiments.

(B) 3T3-L1 adipocytes treated with rAIM for 3 hr were costained for AIM (red) and early, late, or recycling endosomes (green: with antibody to EEA1, Rab7, or Rab11, respectively); AIM (green) and lysosomes (red: LysoTracker Red DND-99); and AIM (green) and lipid droplets (red: Nile Red). Specimens were observed under a confocal microscope.

(C) Electron microscopic analysis of the same cell samples after immunogold labeling of AIM. E, endosome; N, nucleus. Scales are indicated by bars.

(D) Treatment of 3T3-L1 adipocytes with CD36-neutralizing antibody inhibited endocytosis of rAIM. Incorporation of rAIM was assessed in cells treated with α-CD36 antibody or control mouse IgA. A total of 100 cells were evaluated for each treatment. Results were obtained from three independent experiments.

(E) Defective uptake of AIM by $CD36^{-/-}$ adipocytes. rAIM (300 μg/mouse in phosphate-buffered saline) was i.v. injected into $CD36^{+/+}$ and $CD36^{-/-}$ mice. At 16 hr after injection, mice were sacrificed and sections were prepared from epididymal fat tissue. Sections were stained for AIM (green: upper panels) and macrophages F4/80 (red: middle panels).
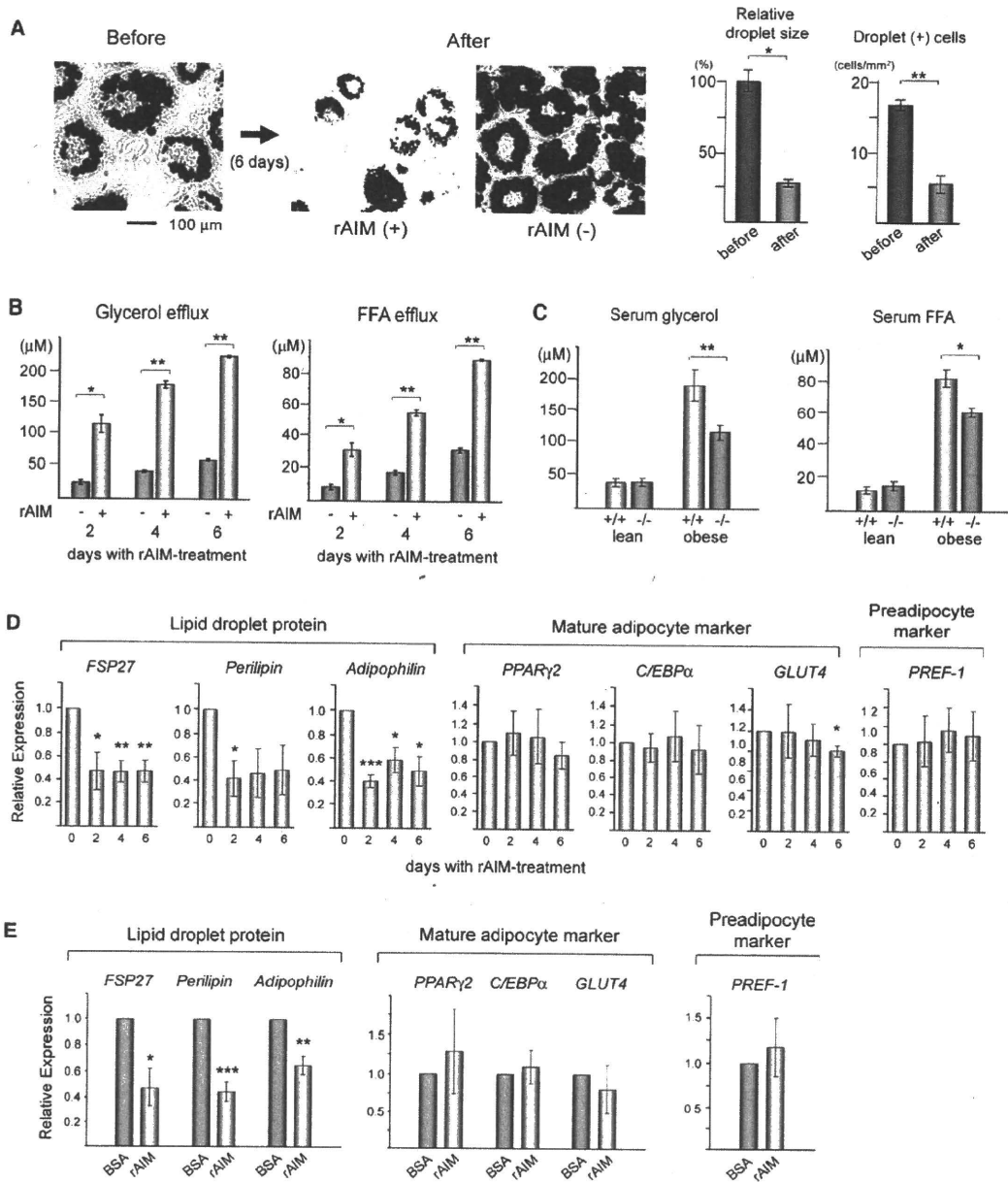
Figure 4. AIM Induces a Lipolytic Response

(A) Differentiated 3T3-L1 adipocytes were challenged with rAIM (5 μg/ml) for 6 days. Cells were stained with Oil Red O before and after rAIM treatment. Representative photomicrographs of cells before and after treatment with or without rAIM (5 μg/ml) are presented. Relative droplet size was assessed by evaluating the diameter of 50 droplets. Error bar indicates SEM. The numbers of droplet-containing cells are also shown (cells/mm²). Data are presented as the means of five independent areas. Error bar indicates SEM. Before, before rAIM treatment; After, after 6 day rAIM treatment.

(B) Efflux of glycerol and FFAs after culture of 3T3-L1 adipocytes with or without rAIM (5 μg/ml) for 2, 4, or 6 days. Data are shown as culture supernatant concentrations. Three independent experiments were performed. Error bar indicates SEM.

(C) Basal levels of glycerol and FFAs in serum from lean (fed with normal chow) and obese (fed with a HFD for 20 weeks) $AIM^{+/+}$ and $AIM^{-/-}$ mice. n = 6 for each group. Error bar indicates SEM.

(D) 3T3-L1 adipocytes incubated with rAIM (5 μg/ml) for 0, 2, 4, or 6 days were analyzed for mRNA levels of FSP27, Perilipin, Adipophilin, PPARγ2, C/EBPα, GLUT4, and PREF-1 by quantitative PCR. Values were normalized to those of glyceraldehyde 3-phosphate dehydrogenase (GAPDH) and presented as relative expression to that for the 0 day rAIM treatment. Three independent experiments were performed. Error bar indicates SEM.

(E) In vivo experiment. The mRNA levels of the same genes as in (D) were assessed by QPCR with RNA isolated from epididymal fat in $AIM^{-/-}$ mice after direct injection of rAIM (100 μg/whole tissue) or BSA (same amount) into the fat tissues (n = 7 for each). Values were normalized to those of GAPDH and presented as relative expression to that from fat tissues injected with BSA. Error bar indicates SEM.
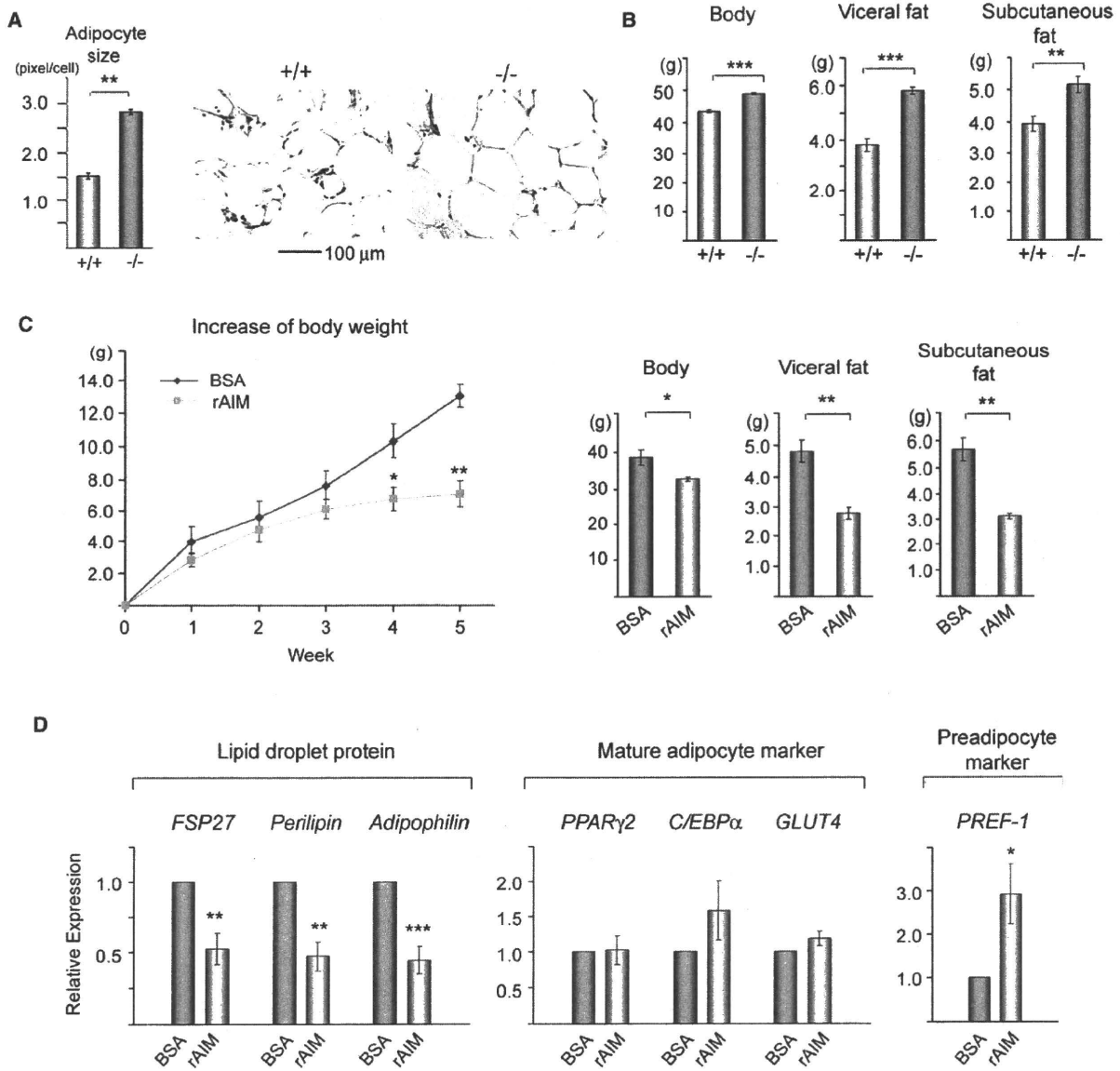
Figure 5. AIM Influences Adipose Tissue Mass

(A) Adipocyte size. In $AIM^{+/+}$ mice (+/+) and $AIM^{-/-}$ mice (−/−) (both fed with a HFD for 20 weeks), epididymal fat sections were stained with H&E, and the diameter of 50 independent adipocytes in different areas was evaluated. Results are presented as averages ± SEM (in pixels). Representative photomicrographs of adipose tissues are also presented.

(B) Weights for body, visceral fat tissue, and subcutaneous fat tissue from $AIM^{+/+}$ mice (+/+) and $AIM^{-/-}$ mice (−/−) fed with a HFD for 12 weeks. n = 7 for $AIM^{+/+}$, and n = 6 for $AIM^{-/-}$. Error bar indicates SEM.

(C) $AIM^{-/-}$ mice were fed with a HFD for 5 weeks, and during the period, they were i.p. injected with rAIM or BSA twice a week (300 μg/injection/mouse). The increase in body weight at each week (line graph) and overall body weight and weight of visceral and subcutaneous fat tissues at the end of experiment (bar graphs) are presented. n = 6 for rAIM-injected mice, and n = 5 for BSA-injected mice. Error bar indicates SEM.

(D) mRNA levels of *FSP27*, *Perilipin* and *Adipophilin*, *PPARγ2*, *C/EBPα*, *GLUT4*, and *PREF-1* were assessed by QPCR with RNA isolated from epididymal fat from mice used in (C) at the end of the experiment. Values were normalized to those of *GAPDH* and presented as relative expression to that of fat tissue injected with BSA. n = 6 for rAIM-injected mice and n = 5 for BSA-injected mice. Error bar indicates SEM.

to the cytoplasm. It is possible that a certain cytosolic chaperone is required, as it has recently been found that the efficient translocation of some proteins across the endosomal membrane is dependent on Hsp90 (Haug et al., 2003; Ratts et al., 2003; Wesche et al., 2006; Giodini and Cresswell, 2008). Additional experiments are necessary to clarify the mechanism responsible for AIM translocation from the endosomal compartment to the cytosol.
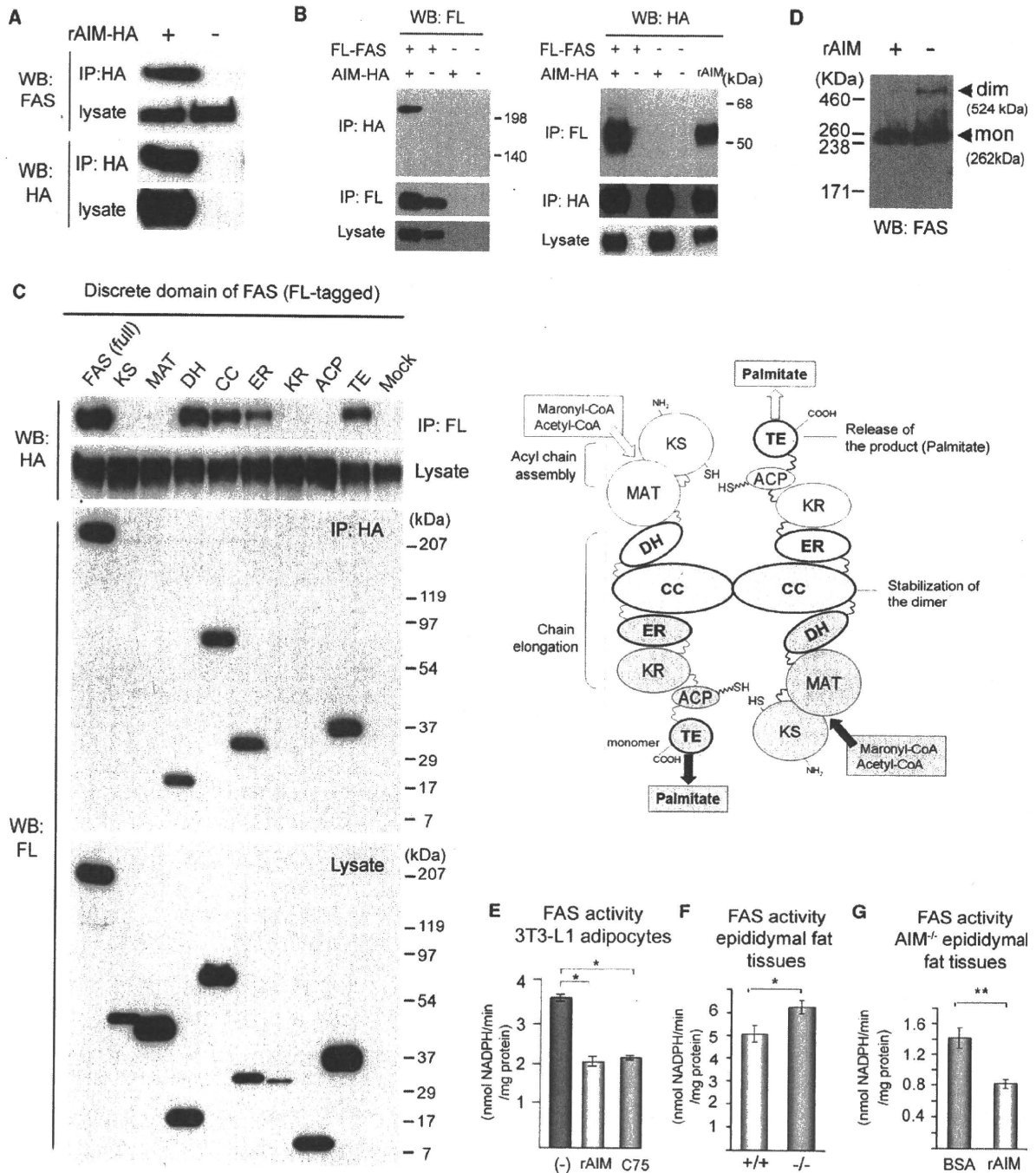
Figure 6. AIM Targets FAS

(A) *AIM*^{-/-} mice were injected with rAIM (HA tagged) directly into the epididymal fat (total 100 μg at several loci). Three hours after injection, fat tissues were used to test the association of incorporated rAIM-HA and endogenous cytosolic FAS in fat tissues via coIP using anti-HA antibody. Precipitates were analyzed for the presence of FAS by western blotting (WB).

(B) Association of rAIM (HA tagged) and FAS (FLAG tagged) in HEK293T cells as determined by coIP assay using anti-Flag or anti-HA antibody.

(C) Left: Each domain of FAS was tagged with the Flag sequence at the N terminus and expressed in HEK293T cells stably expressing AIM-HA, and their association was determined by a coIP assay using anti-Flag or anti-HA antibody. Overexpression of ER or KR domains of FAS resulted in death of a large number of cells. This caused a decrease in WB signals using these cell lysates (lower panels, lanes ER and KR). Results from IP-FL/WB-FL, IP-HA/WB-HA, and IP-control IgG (rat or mouse)/WB-FL or -HA are presented in Figure S6. Right: A schematic of head-to-tail dimerized FAS and descriptions of the major function for each region. Two functional units (distinguished by white and gray) are located on the axis of bound CCs. The AIM-binding domains (DH, CC, ER, and TE) are indicated
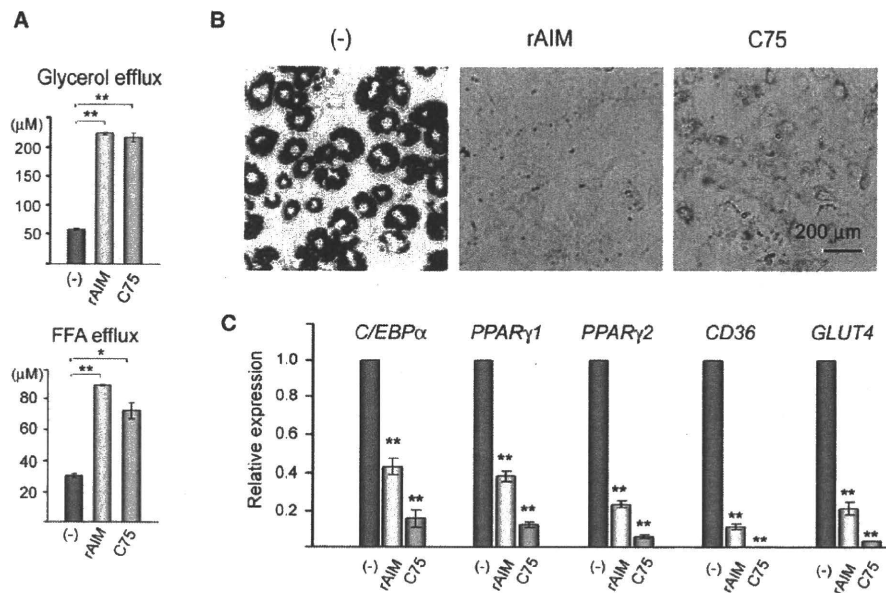
Figure 7. AIM and C75 Exert Comparable Effects on Adipocytes

(A) rAIM (5 µg/ml) or C75 (25 µM) was added to differentiated 3T3-L1 adipocytes for 6 days, and the efflux of glycerol and FFAs was evaluated. Three independent experiments were performed. Error bar indicates SEM.

(B) Both AIM and C75 inhibited adipogenesis. 3T3-L1 preadipocytes were challenged with rAIM (5 µg/ml) or C75 (25 µM) for 2 days during stimulation of differentiation by insulin, DEX, and IBMX. At day 12 of culture, cells were stained with Oil Red O. In the presence of rAIM or C75, adipocyte differentiation was completely prevented.

(C) Gene expression profiles at day 12 of culture. Total RNA was isolated from cells, and the mRNA levels for the indicated genes were assessed by QPCR (n = 3 for each group). Values were normalized to those of *GAPDH* and presented as relative expression to that of cells cultured in the absence of rAIM or C75. Error bar indicates SEM.

FAS as a Target Molecule of Incorporated AIM in Adipocytes

It is of interest that a functional target of AIM is FAS. Through association with multiple regions of FAS (Figure 6C), AIM appears to decrease FAS activity functionally and structurally. The effect of FAS inhibition on the hypothalamus, which influences the fat mass in the body, has been studied extensively. Evidence indicates that systemic administration of C75 decreases the production of neuropeptide Y (NP-Y) in the hypothalamus in mice, resulting in a marked loss of appetite and overall decreased body weight (Loftus et al., 2000; Makimura et al., 2001; Kumar et al., 2002; Mobbs and Makimura, 2002; Shimokawa et al., 2002; Kovacs et al., 2004; Liu et al., 2004; Ronnett et al., 2005; Chakravarthy et al., 2009a). However, $AIM^{-/-}$ and $AIM^{+/+}$ mice showed comparable levels of food intake (Figure S5), suggesting that AIM may not have a neurologic effect. This may be due to the requirement of a specific endocytotic process mediated by CD36, the expression of which is not reported in hypothalamic cells.

Instead, our present results indicate a direct effect of FAS inhibition on adipocytes (brought about by either AIM or C75), which decreases the size and number of lipid droplets, thereby decreasing adipocyte size. There are several possibilities for the mechanism of FAS inhibition in the lipolytic response. Because the inhibition of FAS did not stimulate the cAMP/PKA signaling cascade (Figure S8), it might activate an unknown cAMP/PKA-independent lipolytic pathway. Alternatively, because differentiating adipocytes or mice on a HFD undergo progressive lipogenesis (increase in lipid droplet storage) and constitutive (basal) lipolysis at a substantial level (Holm, 2003; Zechner et al., 2005; Duncan et al., 2007; Lafontan, 2008), the lipolytic outcome on FAS inhibition might simply represent an acute disturbance of lipogenesis. Indeed, it is well known that de novo synthesis of fatty acids via FAS is indispensable for efficient lipogenesis

in bold. A monomer FAS molecule is indicated by a shadowed square. KS, ketoacyl synthase; MAT, malonyl/acetyl transferase; DH, dehydrase; CC, central core; ER, enoylreductase; KR, ketoreductase; ACP, acyl carrier protein; TE, thioesterase.

(D) Dimerized FAS is decreased in the presence of AIM. Cell lysates from 3T3-L1 adipocytes maintained with or without rAIM (5 µg/ml) for 2 days were run on a Tris-acetate gel, and immunoblotting was carried out to assess dimerized (524 kDa) and monomeric (262 kDa) FAS. Sodium dodecyl sulfate (SDS) was removed from the loading buffer to limit potential degradation of the dimerized form.

(E–G) FAS activity in 3T3-L1 adipocytes treated with or without rAIM (5 µg/ml) or C75 (25 µM) for 6 days (E), epididymal fat tissues from $AIM^{+/+}$ and $AIM^{-/-}$ mice (F), and $AIM^{-/-}$ epididymal fat tissue challenged with a local intrafat injection of rAIM or BSA (total 100 µg for each at several loci within the tissue) 3 hr before analysis (G). All mice were fed with a HFD for 20 weeks. Samples were lysed and analyzed for FAS activity. Data are presented for normalized FAS protein levels as assessed by WB using the same samples (data not shown). n = 6 for each group. Error bar indicates SEM.

(Lafontan, 2008). Further discussion related to this issue appears in the Supplemental Information online.

Same Mechanism for Different Functions?

Whether other functions of AIM, in particular its antiapoptotic effect, are carried out by the same molecular mechanism as that in adipocytes will need to be addressed. As shown in Figure 2B, macrophages also incorporate exogenous AIM, suggesting that AIM functions in macrophages in a manner similar to that in adipocytes. Intriguingly, although AIM inhibits apoptosis in macrophages (Miyazaki et al., 1999; Arai et al., 2005), evidence has shown that suppression of FAS promoted apoptosis in some cancer cells (Lupu and Menendez, 2006; Menendez and Lupu, 2007). However, whether apoptosis is inhibited or accelerated by the suppression of FAS might be dependent on cell type. Certainly, in some cell types, the overexpression of FAS accelerated apoptosis, upregulating the expression of proapoptotic genes (J.K. and T.M., unpublished data). Alternatively, intracellular target molecules of AIM may vary in different cell types and/or in different situations. The mediators for AIM internalization might also vary, given that thymocytes and NK-T cells, in which AIM is also effective (Miyazaki et al., 1999; Kuwata et al., 2003), do not express CD36. This may explain the multiple functions observed for AIM in many cell types.

Perspectives

In conclusion, we have identified a function of AIM, along with its molecular mechanism, with respect to adipocyte status in fat tissue. The effects of AIM on other organs important for metabolism, such as liver and muscle, remain to be determined. Further investigation will provide new insights into the role of AIM in the pathogenesis of obesity as well as metabolic diseases.

EXPERIMENTAL PROCEDURES

Mice

$AIM^{-/-}$ mice (Miyazaki et al., 1999) had been backcrossed to C57BL/6 (B6) for 13 generations before being used for experiments. $CD36^{-/-}$ mice (Febbraio et al., 1999) were created and maintained by Febbraio in the Lerner Research Institute, Cleveland Clinic Foundation. All mice were maintained under a specific pathogen-free (SPF) condition.

Statistical Analysis

A two-tailed Mann-Whitney test was used to calculate p values. ***p < 0.001, **p < 0.01, *p < 0.05. Error bars indicate SEM.

Detailed description about reagents for histological analysis, purification of rAIM, in vitro adipogenesis, FAS constructs, efflux analysis of glycerol and FFAs, silver-intensified immunogold for electron microscopy, FAS activity assay, analysis of metabolic rates, quantitative PCR assay, and primers used for experiments appears in the Supplemental Information online.

SUPPLEMENTAL INFORMATION

Supplemental Information includes Supplemental Discussion, Supplemental Experimental Procedures, Supplemental References, and eight figures and can be found with this article online at doi:10.1016/j.cmet.2010.04.013.

ACKNOWLEDGMENTS

REFERENCES

Ackerman, A.L., Kyritsis, C., Tampé, R., and Cresswell, P. (2005). Access of soluble antigens to the endoplasmic reticulum can explain cross-presentation by dendritic cells. Nat. Immunol. 6, 107–113.

Apovian, C.M., Bigornia, S., Mott, M., Meyers, M.R., Ulloor, J., Gagua, M., McDonnell, M., Hess, D., Joseph, L., and Gokce, N. (2008). Adipose macrophage infiltration is associated with insulin resistance and vascular endothelial dysfunction in obese subjects. Arterioscler. Thromb. Vasc. Biol. 28, 1654–1659.

Arai, S., Shelton, J.M., Chen, M., Bradley, M.N., Castrillo, A., Bookout, A.L., Mak, P.A., Edwards, P.A., Mangelsdorf, D.J., Tontonoz, P., and Miyazaki, T. (2005). A role for the apoptosis inhibitory factor AIM/Spalpha/Api6 in atherosclerosis development. Cell Metab. 1, 201–213.

Asturias, F.J., Chadick, J.Z., Cheung, I.K., Stark, H., Witkowski, A., Joshi, A.K., and Smith, S. (2005). Structure and molecular organization of mammalian fatty acid synthase. Nat. Struct. Mol. Biol. 12, 225–232.

Baker, J.L., Olsen, L.W., and Sørensen, T.I. (2007). Childhood body-mass index and the risk of coronary heart disease in adulthood. N. Engl. J. Med. 357, 2329–2337.

Brake, D.K., Smith, E.O., Mersmann, H., Smith, C.W., and Robker, R.L. (2006). ICAM-1 expression in adipose tissue: effects of diet-induced obesity in mice. Am. J. Physiol. Cell Physiol. 291, C1232–C1239.

Chakravarthy, M.V., Zhu, Y., Yin, L., Coleman, T., Pappan, K.L., Marshall, C.A., McDaniel, M.L., and Semenkovich, C.F. (2009a). Inactivation of hypothalamic FAS protects mice from diet-induced obesity and inflammation. J. Lipid Res. 50, 630–640.

Chirala, S.S., Chang, H., Matzuk, M., Abu-Elheiga, L., Mao, J., Mahon, K., Finegold, M., and Wakil, S.J. (2003). Fatty acid synthesis is essential in embryonic development: fatty acid synthase null mutants and most of the heterozygotes die in utero. Proc. Natl. Acad. Sci. USA 100, 6358–6363.

Cinti, S., Mitchell, G., Barbatelli, G., Murano, I., Ceresi, E., Faloia, E., Wang, S., Fortier, M., Greenberg, A.S., and Obin, M.S. (2005). Adipocyte death defines macrophage localization and function in adipose tissue of obese mice and humans. J. Lipid Res. 46, 2347–2355.

Ducharme, N.A., and Bickel, P.E. (2008). Lipid droplets in lipogenesis and lipolysis. Endocrinology 149, 942–949.

Duncan, R.E., Ahmadian, M., Jaworski, K., Sarkadi-Nagy, E., and Sul, H.S. (2007). Regulation of lipolysis in adipocytes. Annu. Rev. Nutr. 27, 79–101.

Farmer, S.R. (2006). Transcriptional control of adipocyte formation. Cell Metab. 4, 263–273.

Febbraio, M., Abumrad, N.A., Hajjar, D.P., Sharma, K., Cheng, W., Pearce, S.F., and Silverstein, R.L. (1999). A null mutation in murine CD36 reveals an important role in fatty acid and lipoprotein metabolism. J. Biol. Chem. 274, 19055–19062.

Finn, P.F., and Dice, J.F. (2006). Proteolytic and lipolytic responses to starvation. Nutrition 22, 830–844.

Gangadharan, B., Antrobus, R., Dwek, R.A., and Zitzmann, N. (2007). Novel serum biomarker candidates for liver fibrosis in hepatitis C patients. Clin. Chem. 53, 1792–1799.

Gebe, J.A., Kiener, P.A., Ring, H.Z., Li, X., Francke, U., and Aruffo, A. (1997). Molecular cloning, mapping to human chromosome 1 q21-q23, and cell binding characteristics of Spalpha, a new member of the scavenger receptor cysteine-rich (SRCR) family of proteins. J. Biol. Chem. 272, 6151–6158.

Gebe, J.A., Llewellyn, M., Hoggatt, H., and Aruffo, A. (2000). Molecular cloning, genomic organization and cell-binding characteristics of mouse Spalpha. Immunology 99, 78–86.

Giodini, A., and Cresswell, P. (2008). Hsp90-mediated cytosolic refolding of exogenous proteins internalized by dendritic cells. EMBO J. 27, 201–211.

Gray, J., Chattopadhyay, D., Beale, G.S., Patman, G.L., Miele, L., King, B.P., Stewart, S., Hudson, M., Day, C.P., Manas, D.M., and Reeves, H.L. (2009). A proteomic strategy to identify novel serum biomarkers for liver cirrhosis and hepatocellular cancer in individuals with fatty liver disease. BMC Cancer 9, 271.

Greenwalt, D.E., Lipsky, R.H., Ockenhouse, C.F., Ikeda, H., Tandon, N.N., and Jamieson, G.A. (1992). Membrane glycoprotein CD36: a review of its roles in adherence, signal transduction, and transfusion medicine. Blood 80, 1105–1115.

Haug, G., Leemhuis, J., Tiemann, D., Meyer, D.K., Aktories, K., and Barth, H. (2003). The host cell chaperone Hsp90 is essential for translocation of the binary Clostridium botulinum C2 toxin into the cytosol. J. Biol. Chem. 278, 32266–32274.

He, W., Barak, Y., Hevener, A., Olson, P., Liao, D., Le, J., Nelson, M., Ong, E., Olefsky, J.M., and Evans, R.M. (2003). Adipose-specific peroxisome proliferator-activated receptor gamma knockout causes insulin resistance in fat and liver but not in muscle. Proc. Natl. Acad. Sci. USA 100, 15712–15717.

Holm, C. (2003). Molecular mechanisms regulating hormone-sensitive lipase and lipolysis. Biochem. Soc. Trans. 31, 1120–1124.

Ibrahimi, A., and Abumrad, N.A. (2002). Role of CD36 in membrane transport of long-chain fatty acids. Curr. Opin. Clin. Nutr. Metab. Care 5, 139–145.

Joseph, S.B., Bradley, M.N., Castrillo, A., Bruhn, K.W., Mak, P.A., Pei, L., Hogenesch, J., O'connell, R.M., Cheng, G., Saez, E., et al. (2004). LXR-dependent gene expression is important for macrophage survival and the innate immune response. Cell 119, 299–309.

Kelley, D.S., Nelson, G.J., and Hunt, J.E. (1986). Effect of prior nutritional status on the activity of lipogenic enzymes in primary monolayer cultures of rat hepatocytes. Biochem. J. 235, 87–90.

Kim, W.K., Hwang, H.R., Kim, H., Lee, P.Y., In, Y.J., Ryu, H.Y., Park, S.G., Bae, K.H., and Lee, S.C. (2008). Glycoproteomic analysis of plasma from patients with atopic dermatitis: CD5L and ApoE as potential biomarkers. Exp. Mol. Med. 40, 677–685.

Kovacs, P., Harper, I., Hanson, R.L., Infante, A.M., Bogardus, C., Tataranni, P.A., and Baier, L.J. (2004). A novel missense substitution (Val1483Ile) in the fatty acid synthase gene (FAS) is associated with percentage of body fat and substrate oxidation rates in nondiabetic Pima Indians. Diabetes 53, 1915–1919.

Kuhajda, F.P., Pizer, E.S., Li, J.N., Mani, N.S., Frehywot, G.L., and Townsend, C.A. (2000). Synthesis and antitumor activity of an inhibitor of fatty acid synthase. Proc. Natl. Acad. Sci. USA 97, 3450–3454.

Kumar, M.V., Shimokawa, T., Nagy, T.R., and Lane, M.D. (2002). Differential effects of a centrally acting fatty acid synthase inhibitor in lean and obese mice. Proc. Natl. Acad. Sci. USA 99, 1921–1925.

Kuwata, K., Watanabe, H., Jiang, S.Y., Yamamoto, T., Tomiyama-Miyaji, C., Abo, T., Miyazaki, T., and Naito, M. (2003). AIM inhibits apoptosis of T cells and NKT cells in Corynebacterium-induced granuloma formation in mice. Am. J. Pathol. 162, 837–847.

Lafontan, M. (2008). Advances in adipose tissue metabolism. Int. J Obes. (Lond) 32 (Suppl 7), S39–S51.

Lin, S.Y., Makino, K., Xia, W., Matin, A., Wen, Y., Kwong, K.Y., Bourguignon, L., and Hung, M.C. (2001). Nuclear localization of EGF receptor and its potential new role as a transcription factor. Nat. Cell Biol. 3, 802–808.

Liu, L.H., Wang, X.K., Hu, Y.D., Kang, J.L., Wang, L.L., and Li, S. (2004). Effects of a fatty acid synthase inhibitor on adipocyte differentiation of mouse 3T3-L1 cells. Acta Pharmacol. Sin. 25, 1052–1057.

Loftus, T.M., Jaworsky, D.E., Frehywot, G.L., Townsend, C.A., Ronnett, G.V., Lane, M.D., and Kuhajda, F.P. (2000). Reduced food intake and body weight in mice treated with fatty acid synthase inhibitors. Science 288, 2379–2381.

Lupu, R., and Menendez, J.A. (2006). Pharmacological inhibitors of Fatty Acid Synthase (FASN)—catalyzed endogenous fatty acid biogenesis: a new family of anti-cancer agents? Curr. Pharm. Biotechnol. 7, 483–493.

Madsen, L., Petersen, R.K., Sørensen, M.B., Jørgensen, C., Hallenborg, P., Pridal, L., Fleckner, J., Amri, E.Z., Krieg, P., Furstenberger, G., et al. (2003). Adipocyte differentiation of 3T3-L1 preadipocytes is dependent on lipoxygenase activity during the initial stages of the differentiation process. Biochem. J. 375, 539–549.

Makimura, H., Mizuno, T.M., Yang, X.J., Silverstein, J., Beasley, J., and Mobbs, C.V. (2001). Cerulenin mimics effects of leptin on metabolic rate, food intake, and body weight independent of the melanocortin system, but unlike leptin, cerulenin fails to block neuroendocrine effects of fasting. Diabetes 50, 733–739.

Menendez, J.A., and Lupu, R. (2007). Fatty acid synthase and the lipogenic phenotype in cancer pathogenesis. Nat. Rev. Cancer 7, 763–777.

Miyazaki, T., Hirokami, Y., Matsuhashi, N., Takatsuka, H., and Naito, M. (1999). Increased susceptibility of thymocytes to apoptosis in mice lacking AIM, a novel murine macrophage-derived soluble factor belonging to the scavenger receptor cysteine-rich domain superfamily. J. Exp. Med. 189, 413–422.

Mobbs, C.V., and Makimura, H. (2002). Block the FAS, lose the fat. Nat. Med. 8, 335–336.

Neels, J.G., and Olefsky, J.M. (2006). Inflamed fat: what starts the fire? J. Clin. Invest. 116, 33–35.

Nishino, N., Tamori, Y., Tateya, S., Kawaguchi, T., Shibakusa, T., Mizunoya, W., Inoue, K., Kitazawa, R., Kitazawa, S., Matsuki, Y., et al. (2008). FSP27 contributes to efficient energy storage in murine white adipocytes by promoting the formation of unilocular lipid droplets. J. Clin. Invest. 118, 2808–2821.

Olshansky, S.J., Passaro, D.J., Hershow, R.C., Layden, J., Carnes, B.A., Brody, J., Hayflick, L., Butler, R.N., Allison, D.B., and Ludwig, D.S. (2005). A potential decline in life expectancy in the United States in the 21st century. N. Engl. J. Med. 352, 1138–1145.

Olsnes, S., Klingenberg, O., and Wiedłocha, A. (2003). Transport of exogenous growth factors and cytokines to the cytosol and to the nucleus. Physiol. Rev. 83, 163–182.

Puri, V., and Czech, M.P. (2008). Lipid droplets: FSP27 knockout enhances their sizzle. J. Clin. Invest. 118, 2693–2696.

Qu, P., Du, H., Li, Y., and Yan, C. (2009). Myeloid-specific expression of Api6/AIM/Sp alpha induces systemic inflammation and adenocarcinoma in the lung. J. Immunol. 182, 1648–1659.

Ratts, R., Zeng, H., Berg, E.A., Blue, C., McComb, M.E., Costello, C.E., vanderSpek, J.C., and Murphy, J.R. (2003). The cytosolic entry of diphtheria toxin catalytic domain requires a host cell cytosolic translocation factor complex. J. Cell Biol. 160, 1139–1150.

Ronnett, G.V., Kim, E.K., Landree, L.E., and Tu, Y. (2005). Fatty acid metabolism as a target for obesity treatment. Physiol. Behav. 85, 25–35.

Rosen, E.D., Sarraf, P., Troy, A.E., Bradwin, G., Moore, K., Milstone, D.S., Spiegelman, B.M., and Mortensen, R.M. (1999). PPAR gamma is required for the differentiation of adipose tissue in vivo and in vitro. Mol. Cell 4, 611–617.

Sandvig, K., and van Deurs, B. (2000). Entry of ricin and Shiga toxin into cells: molecular mechanisms and medical perspectives. EMBO J. 19, 5943–5950.

Sandvig, K., and van Deurs, B. (2005). Delivery into cells: lessons learned from plant and bacterial toxins. Gene Ther. 12, 865–872.

Schmid, B., Rippmann, J.F., Tadayyon, M., and Hamilton, B.S. (2005). Inhibition of fatty acid synthase prevents preadipocyte differentiation. Biochem. Biophys. Res. Commun. 328, 1073–1082.

Shimokawa, T., Kumar, M.V., and Lane, M.D. (2002). Effect of a fatty acid synthase inhibitor on food intake and expression of hypothalamic neuropeptides. Proc. Natl. Acad. Sci. USA 99, 66–71.

Shoelson, S.E., Lee, J., and Goldfine, A.B. (2006). Inflammation and insulin resistance. J. Clin. Invest. 116, 1793–1801.

Smas, C.M., and Sul, H.S. (1993). Pref-1, a protein containing EGF-like repeats, inhibits adipocyte differentiation. Cell 73, 725–734.

Smith, S. (1994). The animal fatty acid synthase: one gene, one polypeptide, seven enzymes. FASEB J. 8, 1248–1259.

Smith, S., Stern, A., Randhawa, Z.I., and Knudsen, J. (1985). Mammalian fatty acid synthetase is a structurally and functionally symmetrical dimer. Eur. J. Biochem. 152, 547–555.

Surmi, B.K., and Hasty, A.H. (2008). Macrophage infiltration into adipose tissue: initiation, propagation and remodeling. Future Lipidol. 3, 545–556.

Valledor, A.F., Hsu, L.C., Ogawa, S., Sawka-Verhelle, D., Karin, M., and Glass, C.K. (2004). Activation of liver X receptors and retinoid X receptors prevents bacterial-induced macrophage apoptosis. Proc. Natl. Acad. Sci. USA 101, 17813–17818.

Wesche, J., Małecki, J., Wiedłocha, A., Skjerpen, C.S., Claus, P., and Olsnes, S. (2006). FGF-1 and FGF-2 require the cytosolic chaperone Hsp90 for translocation into the cytosol and the cell nucleus. J. Biol. Chem. 281, 11405–11412.

Wu, Z., Puigserver, P., and Spiegelman, B.M. (1999a). Transcriptional activation of adipogenesis. Curr. Opin. Cell Biol. 11, 689–694.

Wu, Z., Rosen, E.D., Brun, R., Hauser, S., Adelmant, G., Troy, A.E., McKeon, C., Darlington, G.J., and Spiegelman, B.M. (1999b). Cross-regulation of C/EBP alpha and PPAR gamma controls the transcriptional pathway of adipogenesis and insulin sensitivity. Mol. Cell 3, 151–158.

Yusa, S., Ohnishi, S., Onodera, T., and Miyazaki, T. (1999). AIM, a murine apoptosis inhibitory factor, induces strong and sustained growth inhibition of B lymphocytes in combination with TGF-β1. Eur. J. Immunol. 29, 1086–1093.

Zechner, R., Strauss, J.G., Haemmerle, G., Lass, A., and Zimmermann, R. (2005). Lipolysis: pathway under construction. Curr. Opin. Lipidol. 16, 333–340.

Fast and Accurate Ultrasonography
for Visceral Fat Measurement

You Zhou[1], Norihiro Koizumi[1,2], Naoto Kubota[2,3], Takaharu Asano[3],
Kazuhito Yuhashi[3], Takashi Mochizuki[4], Takashi Kadowaki[2,3],
Ichiro Sakuma[1,2], and Hongen Liao[1,2]

[1] Graduate School of Engineering, The University of Tokyo
[2] Translational Systems Biology and Medicine Initiative, The University of Tokyo
[3] Graduate School of Medicine, The University of Tokyo
[4] Aloka Co. Ltd., Japan
{zhouyou,sakuma,liao}@bmpe.t.u-tokyo.ac.jp

Abstract. Visceral fat area (VFA) has close relationship with hypertension, diabetes and cardiovascular disease, and therefore serve as a reliable indicator of these diseases. Abdominal computed tomography (CT) enables precise quantification of the VFA and has been considered as the gold standard for VFA assessment. In this paper, we develope a novel method to quickly and accurately measure the VFA with ultrasonography (US). We evaluated the novel method on five volunteers and the diagnosis procedures lasted less than 30 seconds averagely. The simulation results by our method were compared with VFA estimated by abdominal CT. The correlation coefficient between them was 0.913 for men and 0.858 for women. And the mean deviation of between VFA by CT and by our method was $19.8\ cm^2$ for men and $13.3\ cm^2$ for women.

1 Introduction

The term metabolic syndrome (MS), a combination of medical disorders that increase the risk of chronic diseases such as diabetes, hypertension, and cardiovascular disease, has been adopted by International Diabetes Federation (IDF) in 2006. MS is a major public health problem, the prevalence of which has increased worldwide. Visceral obesity, the excess accumulation of visceral fat deposits mainly around the waist, is thought to be a fundamental pathology for MS in particular. Therefore, accurate measurement of visceral fat represents an important tool in assessing MS.

Visceral fat, also known as organ fat, packes in between internal organs and the torso, as opposed to subcutaneous fat which is found underneath the skin. Since visceral fat is located deep inside the body and mixed with other organs, its accurate assessment has prooven to be challenging work. Abdominal computed tomography (CT) has been considered the most accurate and reproducible technique of body fat measurement, particularly abdominal adipose tissue. Abdominal CT enables accurate quantification of the visceral fat area (VFA) and therefore serves as the gold standard for visceral fat assessment [1]. However, abdominal CT has many drawbacks, including exposure to radiation, lack of simplicity, high cost, and time-consuming.

Due to these limitations, a variety of alternative methods are being used to assess visceral fat amount and distribution. Previous studies have shown that waist circumference (WC), and WC-based indices can perform as some indicators of the level of visceral obesity [2]. These measurements are recommended as a simpler and easier screening method. However, due to the lack of the individual visualization of visceral fat, these methods have fatal drawbacks such as inability to distinguish subcutaneous fat from visceral fat, inability to take into account an individual's specific information, low level of reproducibility in the case of marked obesity, and most important, poor accuracy.

In recent years, simple methods for assessing visceral fat accumulation using ultrasonography (US) have been studied and were further confirmed by strong correlations with CT-detected VFA [3][4]. Ultrasound has many advantages such as non invasive to human bodies, low-cost, easy to be operated, real time and enables the visualization of visceral fat. Therefore, US-based methods show a balance on simplicity and accuracy between abdominal CT and WC-based indices. However, due to the poor image quality and limited visual field of US, the results of the existing US-based methods are still unsatisfactory and need further improvements.

In the study, a fast and accurate method is developed for visceral obesity studies to provided an estimation of the abdominal visceral fat area and distribution using ultrasonography.

2   Method

2.1   Ultrasound Probe Compatible Device

To provide a quick, easy-operated and accurate way to guide the ultrasonographic procedures, three factors are important: 1) Same positions and angles for ultrasound probe on different patients during diagnosis; 2) Distinct markers easy to be observable in US image; 3) Quantitive measurement on patients' curvature of abdomen.

We designed a belt-shaped ultrasound probe compatible device to fulfill these requirements (**Fig.1**). Two kinds of US measurements of visceral fat are taken. Firstly, US-determined visceral fat distance is defined as the distance between the internal face of the rectus abdominis muscle and the centre of the aorta from each diagnostic position. Secondly, the images acquire from the central position were saved for further processing.

Unlike CT, the ultrasound can only provide a limited scope inside one patient's body. The diagnosing angle and position of probe may differ from doctor to doctor due to their own experiences. This belt-shaped device provides doctors a standard which is easy to follow. In the visual field of an abdominal US, due to the flow of blood, the aorta is nearly the most distinct marker for US. Thus, the belt-shaped device is designed to be fixed in the exact position from where the aorta can be observed most clearly. As a result, the diagnosis process will be finished in seconds, which is convenient for patients as well. With an elastic material, this belt-shaped device would bend smoothly and mold to patient's abdomen. It is easy to understand that: a

patient with mild visceral obesity in normal range of waist circumference would have a 'flatter' shape in abdomen, which means that the belt-shaped device will less bend when diagnosing, while a patient with more serious visceral obesity would get a 'plumper' waist, and resultingly more bent the belt-shaped device becomes when diagnosing. Hence, the curvature of the belt is proportional to the curvature of abdomen, which can serve as valuable characteristic of individual seriousness level of visceral obesity and give a reasonable classification of patients. With three probe-diagnosing positions rather than one, the curvature of abdomen can be described quantitively.
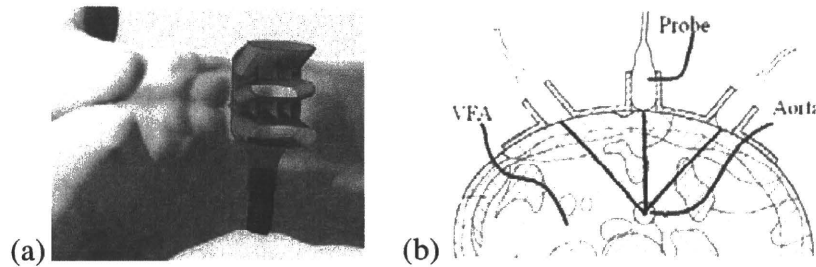

Fig. 1. Ultrasound probe compatible device. Distance and angle between two adjacent probes are 50mm and $40°$ in unbent situation. (a) Belt-shaped device design (b) Measurement method.

2.2   Segmentation of Visceral Fat Area

Analyzed results based on hundreds of abdominal CT images show that most visceral area of patient in his/her abdominal cross-section could be simulated as an ellipse, with aorta in the center. Although this approach may not be very exact for individual patient, the eccentricity of ellipse reflects the curvature of abdomen and therefore serves as a quantitive description of visceral obesity.

The ultrasound probe were detecting from three positions by the belt-shaped device. The information we can acquire contains: b, denotes the distance between the internal face of the rectus abdominis muscle and the centre of the aorta detected from front,   and is defined as semi-minor axis of ellipse; b', denotes the distance between front-end of ultrasound probe in the central diagnosing position and the centre of the aorta detected from front, r, denotes the same distance detected from one side; h', denotes the distance between two probes (50mm); h, denotes the curve length between b and r derived from h' by $h = h'b/b'$ as showed in **Fig. 2(a)**. Then, by ellipse circumference and ellipse parametric equation, we can calculate: a, denotes the semi-major axis; θ, denotes the angle between two probes.

For abdominal cross-section of a patient who has been diagnosed (denotes as patient*), we discretize the visceral area based on the ellipse approach as follow. The ellipse is divided uniformly by angle and axis length. Each section is identified by a number i. For patient*, we define the area of section i as a_i^*, the fat percentage of section i as p_i^* .   Succinctly,   we   have $A^* = (a_1^*, a_2^*, ..., a_n^*)^T$ and $P^* = (p_1^*, p_2^*, ..., p_n^*)^T$, where n refers to the total number of sections (In this paper,

$n \triangleq 30 \times 40 = 1200$). Similar with a matrix, we can define N_i^*, the neighbourhood of p_i^* as: the fat percentages of sections who share the same edges or vertices with section i (**Fig.2(b)**). Immediately, there follows

$$VFA = A^{*T}P^* \ . \tag{1}$$

The computation of A^* is trivial and main difficulty is how to give a reasonable estimation of P^*.

In order to distinguish the visceral fat from other organs, we used a Markov Random Field (MRF) based segmentation algorithm (**Fig. 3**). The main process of this algorithm follows [5]. We must declare here that this kind of algorithms were not developed specially for solving the fat recognition problem of ultrasonographic image, and have never been introduced into this field.
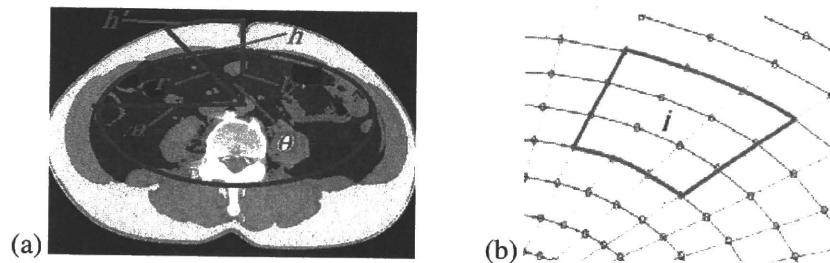

(a)   (b)

Fig. 2. Ellipse approach of abdominal cross-section. (a) Parameters of ellipse. Red part is the visceral fat. Grey part is other organs. (b) Neighbourhood in a discretized ellipse. Green part refers to N_i^*, the neighbourhood of p_i^*.
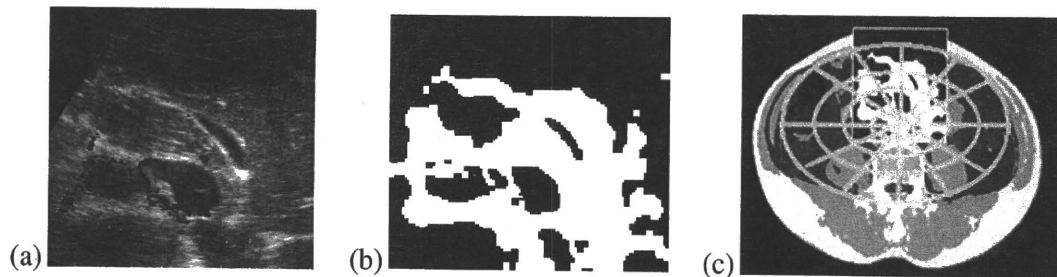

(a)   (b)   (c)

Fig. 3. Distinction of visceral fat. (a) Original US image. The colorful part in central indicates aorta. (b) Segmentation of visceral fat. The white part indicates the visceral fat area. (c) Matching US visual field into the whole visceral area.

2.3   Matching with Pre-stored Data

In this part, we compare the ultrasonographic image of patient∗, with pre-stored CT scanned image of previous patients, and choose the patients whose situations are most similar with the current patient. We established a set V from 146 patients abdominal CT scanned images in a urban hospital, which cover full gamut of patients in its community. This pre-stored CT scanned images served as a pre-stored database with which the current patient∗ can compare.

The visual field of ultrasonography is only local. So, we match the ultrasonography into the whole visceral area, and divide it into m sections following the previous part (**Fig. 3(c)**). We denote section i has area a_i^* and fat percentage p_i^*, for every $i = 1,2,...,m$. We have an estimation of m components of $\boldsymbol{P}^*$, and the problem now is how to estimate the fat percentage of the remaining $(n-m)$ hidden sections $\boldsymbol{P}_h^* = (p_{m+1}^*, p_{m+2}^*, ..., p_n^*)^T$. For CT images, the discretization of ellipse can be accomplished without difficulty. Then, section i of patient k, has the fat percentage P_i^k. Naturally, there is $\boldsymbol{P}^k = (p_1^k, p_2^k, ..., p_n^k)^T$, for $k = 1,2,...,146$.

Now, we want to find out the patients from V whose situations are most similar with patient*. As a result, the visceral fat distributions of those patients would serve as references for patient*. We evaluate the correlative level between patient* and patient k by matching $p_1^*, p_2^*, ..., p_m^*$ and $p_1^k, p_2^k, ..., p_m^k$. We use the Grey-Level Correlation Formula to accomplish it

$$ r^k = \frac{\sum_{i=1}^m (p_i^* - \overline{p^*})(p_i^k - \overline{p^k})}{\sqrt{\sum_{i=1}^m (p_i^* - \overline{p^*})^2 \sum_{i=1}^m (p_i^k - \overline{p^k})^2}} , \tag{2} $$

where $\overline{p^*}$ and $\overline{p^k}$ refer to the average of $p_1^*, p_2^*, ..., p_m^*$ and $p_1^k, p_2^k, ..., p_m^k$ respectively. Before the matching process, the patients whose eccentricity e and minor axis b differ too large from patient* will be rejected in order to accelerate. The 10 patients with max value of r^k compose the set B. The CT image of those chosen patients would serve as the basis of fat estimation of current patient*.

We expect that $\boldsymbol{P}_h^*$ can be expressed as a 'combination' of patients from B and this combination can reflect the visceral fat distribution of patient*. To achieve it, we establish an optimization standard. By (3), we defines the cost at one section, and (4) is the integrally cost, which should be minimized. Consider $N_i^* \subset \boldsymbol{P}^*$, the neighbourhood of p_i^*. We give a choice not only realizing optimization at single p_i^* itself, but also throughout its neighbourhood N_i^*. We define the distance cost function between patient* and patient k at section i as

$$ \left(|p_i^* - p_j^*| - |p_i^k - p_j^k| \right)^2 , \quad p_j^* \in N_i^*, p_j^k \in N_i^k , \tag{3} $$

where N_i^* and N_i^k refers to the neighbourhood of p_j^* and p_j^k respectively. Hence, integrally, the $\boldsymbol{P}_h^*$ should be the vector who satisfies that

$$ arg\ \min_{p_i^* \in P_h^*} \sum_{i=m+1}^n \sum_{k=1}^{10} \sum_{p_j^* \in N_i^*, p_j^k \in N_i^k} \left(|p_i^* - p_j^*| - |p_i^k - p_j^k| \right)^2 , \tag{4} $$

$$ p_i^* \in [0,1], \text{ for } i = 1,2,...,n. $$

Consequently, the determination of $\boldsymbol{P}_h^*$ has been transformed into an optimization problem. This numerical optimization is performed automatically by a constraint nonlinear conjugate gradient method (CGM).

3   Experiment Results

In this part, all correlations between two variables were evaluated using Pearson's product-moment correlation coefficient. Comparisons between each two groups were done with an unpaired t-test.

3.1   Evaluation Experiment of US

We tested the belt-shaped ultrasound probe compatible device on five volunteers from an urban community. All our ultrasonographic procedures were performed by the same examiner using a portable ultrasonography equipment (α10, ALOKA, Japan). The center of the belt-shaped device fixed exactly 2 cm left to umbilicus for each patient. Each patient assumed a supine position, and US data were measured at the end of expiration by a 6-MHz 2D abdominal probe, while the probe was making contact with patients' skin as slight as possible (**Fig.4**).

For each volunteer, the diagnosis procedures lasted less than 30 seconds. This is quite an acceptable time during a medical examination. In addition, More quick diagnosis speed is also expectable in the future if doctors become more proficient in this novel method.
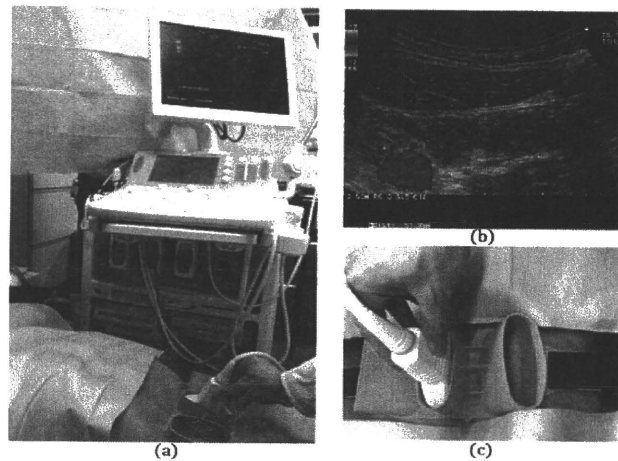

Fig. 4. Practical diagnosis procedures for a patient. (a) Diagnosis by US. (b) Distance of visceral fat measured in US image. (c) Belt-shaped ultrasound probe compatible device.

3.2   Campare with CT Results

Simulation on 146 patients' abdominal CT images were done and showed that there was strong correlation between the US observed VFA from front psotion and the total VFA of an individual patient. The coeffecent was r = 0.883 and the level of significance was p-value < 2.2e-16 (**Fig. 5**). As a result, it is reasonable to use the US observed fat percentage as an indicator for total VFA.

Since abdominal CT holds the most accurate quantification of the VFA, we treated it as the testing standard for visceral fat assessment. Abdominal cross-section by CT scanning was obtained in a single tomographic slice at umbilical level as ultrasound probe did. Portions with a CT number of −200 to −10 Hounsfield Units (HU) were separated as adipose tissue and their areas were automatically calculated.

We simulated our method on 28 male and 35 female samples, and compared the results with abdominal CT. **Figure 6** shows the comparisons of CT and our US-based method. The mean deviation between VFA measured by CT and our US method for each patient is $19.8\ cm^2$ for men and $13.3cm^2$ for women. The correlation between these two groups is also presented. For men, the coeffect was r = 0.913 and the level of significance was p-value = 1.179e-11. For women, there are r = 0.858 and p-value = 4.674e-11. These results proofed the significant positive correlations between VFA measured by CT and by our method.

And we also divided these 63 patients in both sex into three groups by the CT-measured VFA: low ($\le 100cm^2$), medium (between $100cm^2$ and $140cm^2$) and high ($> 140cm^2$). The average and max VFA deviations between US method and CT method of these three groups were shown in **Table 1**. From this table, it is easy to notice that our US-based method performed better on the medium group than other two groups averagely. The reason of this is that the data per-stored data mainly laid mainly in this VFA range. Thus, the result reminds us that the pre-stored database is very essential for our method and it must cover full range of patients in enough quantities. On the other hand, the max VFA deviations are all too large in three groups. This demonstrates that there are many personal detailed characteristics of certain patients have been omitted in our method, which should be checked carefully for the further improvement of this US-based method.
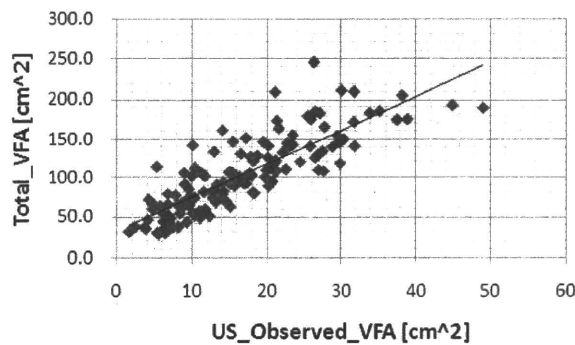

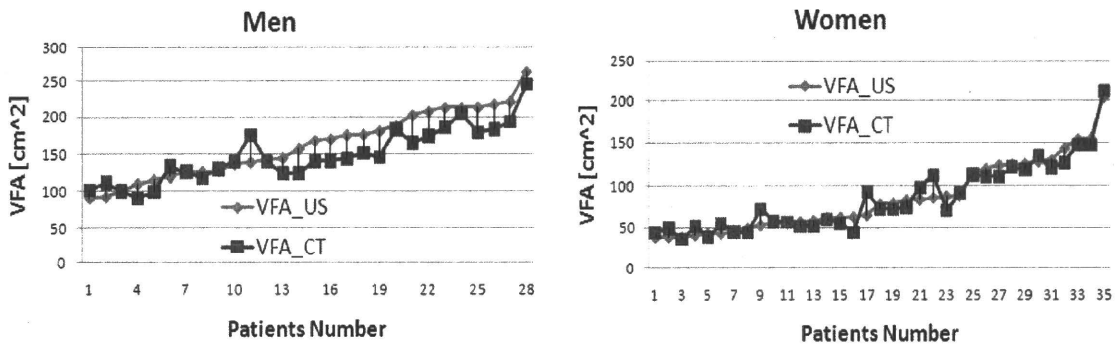**Fig. 5.** Scattergram of relationship between US observed VFA and the total VFA

Fig. 6. Camprison of our US-based method and CT for men and women

Table 1. VFA deviations between US_method and CT_method in different groups

Groups		low	medium	high
Numbers of patients		17	25	21
VFA deviations (cm^2)	Average	15.7	9.1	27.3
	Max	42.2	36.9	37.3

4   Discussions and Conclusion

This paper proposes a novel US-based method for estimation of the VFA. A fast and convenient diagnosis method was introduced and a robust algorithm was proposed to estimate a patient's VFA from US data automatically. As far as we know, this is the first attempt to compute VFA by ultrasound, and our results were shown to be strongly correlated with CT measurements.

However, one main limitation of this present study is that all the data of patients were collected from the same ethnic group. Thus, the results cannot generalize directly to other individuals of certain ethnic groups. For instance, the female body type in particular differs largely between Westerners and Easterners. As a result, how to apply this novel method universally needs further discussions.

Till now, we have developed a US-based method whose accuracy reaches the level of abdominal CT. However, it is not an entirely impossible thing that the US-based method will become a more reliable indicator for MS than abdominal CT in the future. Due to the non-invasiveness and simplity of US, diagnosis at different levels of the abdomen will be accomplished without much difficulties. Consequencely, 3D individual visualization and estimation of   visceral fat can be realized by US, while usually only one slice of abdominal cross-section image can be acquired by CT in medical examination due to the harmness of rediation. Secondly, due to its real-time characteristics, US allows us to detect visceral fat over a period of time. One patient's abdominal cross-sectional area when expiring will differ largely from inspiring. Abdominal CT cannot take this difference into consider and therefore would be less convincing than US in this respect. Further, by US, we may represent a useful method for monitoring weight loss, variations and transfer of visceral fat, which can be expected to indicate the associated risks of MS more accurately.

In conclusion, although its results are still rough and there are many details need discussing, the present US-based method has proofed to be a considerably fast and accurate way for VFA estimation.

Acknowledgment

References

1. Rossner, S., Bo, W.J., Hiltbrandt, E., et al.: Adipose tissue determinations in cadavers—a comparison between cross-sectional planimetry and computed tomography. Int. J. Obes. Relat. Metab. Disord. 14, 893–902 (1990)
2. Hsieh, S.D., Yoshinaga, H., Muto, T.: Waist-to-height ratio, a simple and practical index for assessing central fat distribution and metabolic risk in Japanese men and women. Int. J. Obes. Relat. Metab. Disord. 27, 610–616 (2003)
3. Chiba, Y., Saitoh, S., et al.: Relationship between Visceral Fat and Cardiovascular Disease Risk Factors: The Tanno and Sobetsu Study. Hypertension Research 30, 229–236 (2007)
4. Ribeiro-Filho, F.F., et al.: Methods of Estimation of Visceral Fat: Advantages of Ultrasonography. Obesity Research 11(12), 1488–1494 (2003)
5. Lorenz, A., Haas, C., Ermert, H.: Segmentation of ultrasonic prostate images using a probabilistic model based on Markov random processes. Ultrason Imaging 19, 44–45 (1997)

A Liver-Derived Secretory Protein, Selenoprotein P, Causes Insulin Resistance

Hirofumi Misu,[1,10] Toshinari Takamura,[1,10,*] Hiroaki Takayama,[1] Hiroto Hayashi,[1] Naoto Matsuzawa-Nagata,[1]
Seiichiro Kurita,[1] Kazuhide Ishikura,[1] Hitoshi Ando,[1] Yumie Takeshita,[1] Tsuguhito Ota,[1] Masaru Sakurai,[1]
Tatsuya Yamashita,[1] Eishiro Mizukoshi,[1] Taro Yamashita,[1] Masao Honda,[1] Ken-ichi Miyamoto,[2,3] Tetsuya Kubota,[4]
Naoto Kubota,[4] Takashi Kadowaki,[4] Han-Jong Kim,[5] In-kyu Lee,[5] Yasuhiko Minokoshi,[6] Yoshiro Saito,[7]
Kazuhiko Takahashi,[8] Yoshihiro Yamada,[9] Nobuyuki Takakura,[9] and Shuichi Kaneko[1]
[1]Department of Disease Control and Homeostasis
[2]Department of Hospital Pharmacy
[3]Department of Medicinal Informatics
Kanazawa University Graduate School of Medical Science, Kanazawa, Ishikawa 920-8641, Japan
[4]Department of Diabetes and Metabolic Diseases, Graduate School of Medicine, University of Tokyo, Tokyo 113-8655, Japan
[5]Section of Endocrinology, Department of Internal Medicine, Kyungpook National University Hospital, School of Medicine, Kyungpook
National University, Jungu, Daegu 700-412, Korea
[6]Division of Endocrinology and Metabolism, Department of Developmental Physiology, National Institute for Physiological Sciences,
Okazaki, Aichi 444-8585, Japan
[7]Department of Medical Life Systems, Faculty of Medical and Life Sciences, Doshisha University, Kyotanabe, Kyoto 610-0394, Japan
[8]Department of Nutritional Biochemistry, Hokkaido Pharmaceutical University, Otaru, Hokkaido 047-0264, Japan
[9]Department of Signal Transduction, Research Institute for Microbial Diseases, Osaka University, Osaka 565-0871, Japan
[10]These authors contributed equally to this work
*Correspondence: ttakamura@m-kanazawa.jp
DOI 10.1016/j.cmet.2010.09.015

SUMMARY

The liver may regulate glucose homeostasis by modulating the sensitivity/resistance of peripheral tissues to insulin, by way of the production of secretory proteins, termed hepatokines. Here, we demonstrate that selenoprotein P (SeP), a liver-derived secretory protein, causes insulin resistance. Using serial analysis of gene expression (SAGE) and DNA chip methods, we found that hepatic SeP mRNA levels correlated with insulin resistance in humans. Administration of purified SeP impaired insulin signaling and dysregulated glucose metabolism in both hepatocytes and myocytes. Conversely, both genetic deletion and RNA interference-mediated knockdown of SeP improved systemic insulin sensitivity and glucose tolerance in mice. The metabolic actions of SeP were mediated, at least partly, by inactivation of adenosine monophosphate-activated protein kinase (AMPK). In summary, these results demonstrate a role of SeP in the regulation of glucose metabolism and insulin sensitivity and suggest that SeP may be a therapeutic target for type 2 diabetes.

INTRODUCTION

Insulin resistance is an underlying feature of people with type 2 diabetes and metabolic syndrome (Saltiel and Kahn, 2001), but is also associated with risk for cardiovascular diseases (Després et al., 1996) and contributes to the clinical manifestations of nonalcoholic steatohepatitis (Ota et al., 2007). In an insulin-resistant state, impaired insulin action promotes hepatic glucose production and reduces glucose uptake by peripheral tissues, resulting in hyperglycemia. The molecular mechanisms underlying insulin resistance are not fully understood, but are now known to be influenced by the secretion of tissue-derived factors, traditionally considered separate from the endocrine system. Recent work in obesity research, for example, has demonstrated that adipose tissues secrete a variety of proteins, known as adipocytokines (Friedman and Halaas, 1998; Maeda et al., 1996; Scherer et al., 1995; Steppan et al., 2001; Yang et al., 2005), which can either enhance or impair insulin sensitivity, thereby contributing to the development of insulin resistance.

SeP (in humans encoded by the *SEPP1* gene) is a secretory protein primarily produced by the liver (Burk and Hill, 2005; Carlson et al., 2004). It contains ten selenocysteine residues and functions as a selenium supply protein (Saito and Takahashi, 2002). However, the role of SeP in the regulation of glucose metabolism and insulin sensitivity has not yet been established. Furthermore, the clinical significance of SeP in human diseases has not been well defined, although studies of SeP knockout mice showed SeP deficiency to be associated with neurological injury and low fertility (Hill et al., 2003; Schomburg et al., 2003).

The liver plays a central role in glucose homeostasis and is also the site for the production of various secretory proteins. For example, recent work in our laboratory has revealed that genes encoding secretory proteins are abundantly expressed in the livers of people with type 2 diabetes (Misu et al., 2007). Moreover, genes encoding angiogenic factors, fibrogenic factors, and redox-associated factors were differentially expressed in the livers of people with type 2 diabetes (Takamura et al., 2004; Takeshita et al., 2006), possibly contributing to the pathophysiology of

type 2 diabetes and its clinical manifestations. On the basis of these findings, we hypothesize that, analogous to adipose tissues, the liver may also contribute to the development of type 2 diabetes and insulin resistance, through the production of secretory proteins, termed hepatokines.

RESULTS

Identification of a Hepatic Secretory Protein Involved in Insulin Resistance

To identify hepatic secretory proteins involved in insulin resistance, we performed liver biopsies in humans and conducted a comprehensive analysis of gene expression profiles, using two distinct methods. First, we obtained human liver samples from five patients with type 2 diabetes and five nondiabetic subjects who underwent surgical procedures for malignant tumors, and we subjected them to serial analysis of gene expression (SAGE) (Velculescu et al., 1995). Consequently, we identified 117 genes encoding putative secretory proteins with expression levels in people with type 2 diabetes, 1.5-fold or greater higher than those in normal subjects. Next, we obtained ultrasonography-guided percutaneous needle liver biopsies from ten people with type 2 diabetes and seven normal subjects (Table S1 available online), and we subjected them to DNA chip analysis to identify genes whose hepatic expression was significantly correlated with insulin resistance (Table S2). We performed glucose clamp experiments on these human subjects and measured the metabolic clearance rate (MCR) of glucose (glucose infusion rate divided by the steady-state plasma glucose concentration) as a measure of systemic insulin sensitivity. As a result, we found that $SEPP1$ expression levels were upregulated 8-fold in people with type 2 diabetes compared with normal subjects, as determined by SAGE (Table S2). Additionally, there was a negative correlation between hepatic $SEPP1$ messenger RNA (mRNA) levels and the MCR of glucose, indicating that elevated hepatic $SEPP1$ mRNA levels were associated with insulin resistance (Figure 1A). As a corollary, we found a positive correlation between the levels of hepatic $SEPP1$ mRNA and postloaded or fasting plasma glucose (Figures 1B and 1C).

Elevation of SeP in Type 2 Diabetes

To characterize the role of SeP in the development of insulin resistance, we measured serum SeP levels in human samples (Table S3), using enzyme-linked immunosorbent assays (ELISA), as described previously (Saito et al., 2001). Consistent with elevated hepatic $SEPP1$ mRNA levels, we found a significant positive correlation between serum SeP levels and both fasting plasma glucose and hemoglobin A_{1c} (HbA_{1c}) levels (Figures 1D and 1E). HbA_{1c} is a clinical marker of protein glycation due to hyperglycemia, and elevated HbA_{1c} levels generally reflect poor glucose control over a 2–3 month period. Additionally, serum levels of SeP were significantly elevated in people with type 2 diabetes compared with normal subjects (Figure 1F and Table S4). Similar to data derived from clinical specimens, in rodent models of type 2 diabetes, including OLETF rats and KKAy mice, hepatic $Sepp1$ mRNA and serum SeP levels were elevated (Figures 1G–1J and Table S5).

SeP Expression in Hepatocytes Is Regulated by Glucose, Palmitate, and Insulin

To clarify the pathophysiology contributing to the hepatic expression of SeP in type 2 diabetes, we investigated the effects of nutrient supply on $Sepp1$ mRNA expression in cultured hepatocytes. We found that the addition of glucose or palmitate upregulated $Sepp1$ expression, whereas insulin downregulated it in a dose- and time-dependent manner (Figures 2A, 2C, 2E, and 2F). Similar effects on SeP protein levels were observed in primary mouse hepatocytes (Figures 2B, 2D, and 2G). Consistent with the negative regulation of $Sepp1$ by insulin in hepatocytes, $Sepp1$ mRNA levels were elevated in the livers of fasting C57BL6J mice, compared with those that had been fed (Figure 2H). Thus, multiple lines of evidence suggest that elevated SeP is associated with the development of insulin resistance.

SeP Impairs Insulin Signaling and Dysregulates Glucose Metabolism In Vitro

Because there is no existing cell culture or animal model in which SeP is overexpressed, we purified SeP from human plasma using chromatographic methods (Saito et al., 1999; Saito and Takahashi, 2002) to examine the effects of SeP on insulin-mediated signal transduction. Treatment of primary hepatocytes with purified SeP induced a reduction in insulin-stimulated phosphorylation of insulin receptor (IR), and Akt (Figures 3A and 3B). SeP exerts its actions through an increase in cellular glutathione peroxidase (Saito and Takahashi, 2002). Coadministration of BSO, a glutathione synthesis inhibitor, rescued cells from the inhibitory effects of SeP (Figure 3C). Moreover, SeP increased phosphorylation of IRS1 at Ser307, the downregulator of tyrosine phosphorylation of IRS (Figure S1A). Similar effects of SeP were also observed in C2C12 myocytes (Figure S1B). Next, we assessed whether SeP dysregulated cellular glucose metabolism. In H4IIHEC hepatocytes, treatment with SeP upregulated mRNA expression of $Pck1$ and $G6pc$, key gluconeogenic enzymes, resulting in a 30% increase in glucose release in the presence of insulin (Figures 3D–3F). Treatment with SeP alone had no effects on the levels of mRNAs encoding gluconeogenic enzymes or on glucose production in the absence of insulin, suggesting that SeP modulates insulin signaling. Additionally, treatment with SeP induced a reduction in insulin-stimulated glucose uptake in C2C12 myocytes (Figure 3G). These in vitro experiments indicate that, at physiological concentrations, SeP impairs insulin signal transduction and dysregulated cellular glucose metabolism.

SeP Impairs Insulin Signaling and Disrupts Glucose Homeostasis In Vivo

To examine the physiological effects of SeP in vivo, we treated female C57BL/6J mice with two intraperitoneal injections of purified human SeP (1 mg/kg body weight), 12 and 2 hr before the experiments. Injection of purified human SeP protein resulted in serum levels of 0.5–1.5 μg/mL (data not shown). These levels correspond to the incremental change of SeP serum levels in people with normal glucose tolerance to those with type 2 diabetes (Saito et al., 2001). Glucose and insulin tolerance tests revealed that treatment of mice with purified SeP induced glucose intolerance and insulin resistance (Figures 3H and 3I). Blood insulin levels were significantly elevated in
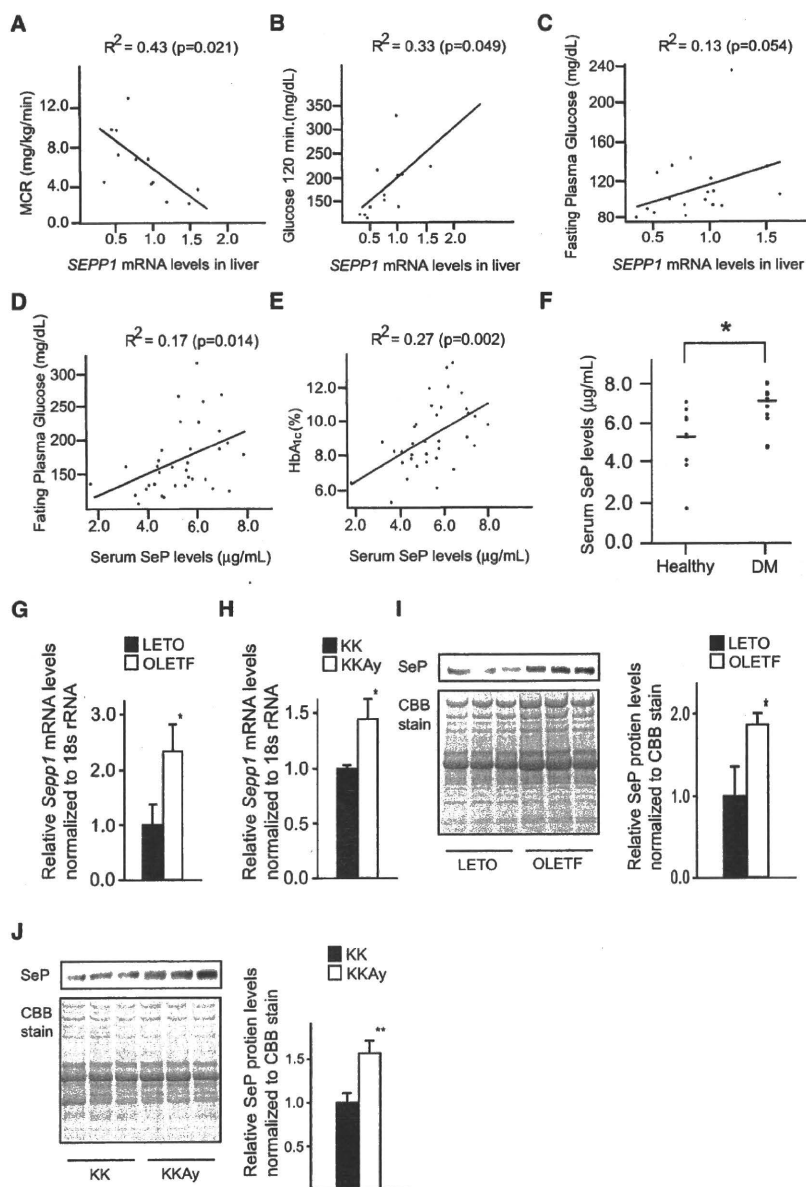
Figure 1. Elevation of Serum SeP Levels and Hepatic Sepp1 Expression in Type 2 Diabetes

(A–C) Individual correlations between hepatic SEPP1 mRNA levels and metabolic clearance rate (MCR) of glucose (A), postloaded plasma glucose levels (B), and fasting plasma glucose levels (C) in humans (n = 12–17). MCR equals the glucose infusion rate divided by the steady-state plasma glucose concentration, and is a measure of systemic insulin sensitivity. MCR values were determined by glucose clamp. SEPP1 mRNA levels were quantified with DNA chips.

(D and E) Correlations between serum levels of SeP and fasting plasma glucose levels (D) and HbA_{1c} (E) in people with type 2 diabetes (n = 35).

(F) Serum levels of SeP in people with type 2 diabetes and healthy subjects (n = 9–12). Age and body weight were not significantly different between the two groups. Data represents the means ± SEM from two groups. *p < 0.05.

(G and H) Hepatic Sepp1 mRNA levels in an animal model of type 2 diabetes (n = 5–6).

(I and J) Serum SeP levels in an animal model of type 2 diabetes. SeP was detected by western blotting. Coomassie brilliant blue (CBB)-stained gel is used as a control for protein loading. Graphs display the results of densitometric quantification, normalized to CBB-stained proteins (n = 5).

Data represent the mean ± SEM from five to six mice per group. *p < 0.05, **p < 0.01. See also Tables S1–S5.

Knockdown of Sepp1 in Liver Improves Glucose Intolerance and Insulin Resistance in Mice with Type 2 Diabetes

To determine whether knockdown of endogenous Sepp1 enhances insulin signaling, we transfected H4IIEC hepatocytes with Sepp1-specific small interfering RNA (siRNA), and we observed a reduction in endogenous Sepp1 mRNA and SeP protein levels (Figures 4A and 4B). Insulin-stimulated serine phosphorylation of Akt was enhanced in these treated cells (Figure 4C). Similarly, delivery of Sepp1-specific siRNAs into KKAy mice via a hydrodynamic transfection method (McCaffrey et al., 2002; Zender et al., 2003) resulted in a 30% reduction in SeP protein levels in the liver and blood (Figures 4D–4G and Figure S2). Knockdown of Sepp1 improved both glucose intolerance (Figures 4H and 4I) and insulin resistance (Figures 4J and 4K) in KKAy mice.

SeP-Deficient Mice Show Improved Glucose Tolerance and Enhanced Insulin Signaling in Liver and Muscle

We further confirmed the long-term effects of lowered SeP using Sepp1 knockout mice (Hill et al., 2003). SeP knockout mice were viable and displayed normal body weights when maintained on a selenium-sufficient diet. Body weight, food intake, and O_2 consumption were unaffected by SeP knockout (Figures S3A

SeP-injected mice, although those of glucagon and GLP-1 were unaffected during a glucose tolerance test (Figure S1C). Western blot analysis showed a reduction in insulin-induced serine phosphorylation of Akt in both liver and skeletal muscle of SeP-injected mice (Figures 3J and 3K). Hyperinsulinemic-euglycemic clamp studies showed that treatment with SeP significantly increased endogenous glucose production and decreased peripheral glucose disposal (Figure S1D and Figures 3L and 3M). Additionally, serum levels of injected human SeP protein negatively correlated with rates of peripheral glucose disposal (Figure S1E). These data indicate that SeP impairs insulin signaling in the liver and skeletal muscle and induces glucose intolerance in vivo.